Micromagnetic simulations of rst-order reversal curve (FORC) diagrams of framboidal greigite

Micromagnetic simulations of first-order reversal curve (FORC) diagrams of framboidal greigite

Miguel A. Valdez-Grijalva[a,*], Lesleis Nagy[b], Adrian R. Muxworthy[a,**], Wyn Williams[c], Andrew P. Roberts[d], David Heslop[d]

[a] *Department of Earth Science and Engineering, Imperial College London, London, SW7 2BP, UK*
[b] *Geosciences Research Division, Scripps Institution of Oceanography, La Jolla, CA 92037, USA*
[c] *School of GeoSciences, University of Edinburgh, Edinburgh, EH9 3FE, UK*
[d] *Research School of Earth Sciences, Australian National University, Canberra, ACT 2601, Australia*

Abstract

Greigite is a sensitive environmental indicator and occurs commonly in nature as magnetostatically interacting framboids. Until now only the magnetic response of isolated non-interacting greigite particles have been modelled micromagnetically. We present here hysteresis and first-order reversal curve (FORC) simulations for framboidal greigite (Fe_3S_4), and compare results to those for isolated particles of a similar size. We demonstrate that these magnetostatic interactions alter significantly the framboid FORC response compared to isolated particles, which makes the magnetic response similar to that of much larger (multidomain) grains. We also demonstrate that framboidal signals plot in different regions of a FORC diagram, which facilitates differentiation between framboidal and isolated grain signals. Given that

[*] Now at Instituto Mexicano del Petróleo, Mexico City, 07730, Mexico
[**] corresponding author
Email address: adrian.muxworthy@imperial.ac.uk (Adrian R. Muxworthy)

large greigite crystals are rarely observed in microscopy studies of natural samples, we suggest that identification of multidomain-like FORC signals in samples known to contain abundant greigite could be interpreted as evidence for framboidal greigite.

Keywords: greigite, framboid, micromagnetic simulation, FORC diagram
PACS: 91.25.F-, 91.60.Pn, 91.25.fa

---

1. Introduction

Greigite (Fe_3S_4) is an authigenic ferrimagnetic mineral found in sediments (Roberts et al., 2011). It occurs in sulphate-reducing environments, and is an indicator that sulphate reduction has occurred (Roberts, 2015). It is most commonly found in strongly interacting, close-packed clusters called framboids (Ariztegui and Dobson, 1996; Roberts et al., 2011). It often co-occurs with authigenic pyrite (FeS_2) framboids, where greigite framboids can grow before or after formation of an original generation of pyrite framboids (Rowan and Roberts, 2006; Rowan et al., 2009).

The magnetic structure and stability of isolated greigite particles have been the subject of previous numerical studies (Muxworthy et al., 2013; Valdez-Grijalva et al., 2018a,b). These studies examined the effect of grain size, and identified the transition size for stable single-domain (SD) to single-vortex (SV) behaviour ($\sim 54 - 70\,\mathrm{nm}$ for equidimensional grains); at this threshold size the magnetic structure becomes non-uniform and the magnetic response changes markedly. Numerical simulations have been performed for hysteresis and first-order reversal curve (FORC) properties of non-interacting SD and SV greigite dispersions (Valdez-Grijalva et al., 2018a; Valdez-Grijalva

and Muxworthy, 2019); however, the FORC properties of highly interacting greigite ensembles remain poorly understood. FORC diagrams are routinely used in environmental magnetism and palaeomagnetism to identify magnetic minerals (Roberts et al., 2014, 2018b). Muxworthy et al. (2013) made threshold transition calculations for linear chains of magnetostatically interacting greigite; however, such linear chains are only observed in magnetotactic bacteria. Inorganic greigite often occurs as framboidal clusters, so the findings of Muxworthy et al. (2013) cannot be applied directly to framboids. Given that natural framboidal structures are found commonly in greigite and magnetite (e.g., Rowan and Roberts, 2006; Emmerton et al., 2013), there is a need to understand their magnetic hysteresis loops and FORC signatures. The magnetic moments of individual framboids are too small to measure, so we must develop numerical models to isolate their signals.

In this paper, we use a numerical micromagnetic finite element method (FEM) model to calculate the FORC response of framboidal greigite composed of highly interacting, close-packed 30 nm grains. At this size, isolated equidimensional grains can only occur in the SD state (Valdez-Grijalva et al., 2018a) and produce FORC signals characteristic of isolated SD grains with cubic magnetocrystalline anisotropy (Valdez-Grijalva et al., 2018a).

2. Methods

2.1. The micromagnetic method

The numerical micromagnetic MERRILL FEM model (Ó Conbhuí et al., 2018) was used here to calculate FORC diagrams for strongly interacting greigite clusters. A ferromagnetic (*sensu lato*) material has a Gibbs free-

energy E_G, which excluding the effects of thermal fluctuations and magnetostriction, can be written as (Brown, 1963):

$$E_{\mathrm{G}} = \int_{\Omega} (\phi_{\mathrm{exchange}} + \phi_{\mathrm{anisotropy}} + \phi_{\mathrm{stray}} + \phi_{\mathrm{external}})\, \mathrm{d}\Omega, \tag{1}$$

where Ω is the ferromagnetic volume, so that integration is carried out over the ferromagnetic body. The ϕ terms are described below. First, the exchange energy (ϕ_{exchange}) is given by;

$$\phi_{\mathrm{exchange}} = A|\nabla \boldsymbol{m}|^2, \tag{2}$$

where $\boldsymbol{m}$ is the reduced (unitary) magnetisation vector and A is the exchange stiffness constant. The exchange energy is an expression that provides a continuum approximation of the energy density due to quantum-mechanical exchange forces between atomic spins (Landau and Lifshitz, 1935).

For greigite, the magnetocrystalline anisotropy energy ($\phi_{\mathrm{anisotropy}}$) is dominated by the first term (K_1) at room temperature (Winklhofer et al., 2014), and the anisotropy energy can be written in terms of the reduced magnetisation:

$$\phi_{\mathrm{anisotropy}} = K_1(m_x^2 m_y^2 + m_y^2 m_z^2 + m_z^2 m_x^2). \tag{3}$$

The magnetic Gibbs free-energy associated with the magnetostatic self-interaction (ϕ_{stray}) of the ferromagnetic body and the stray magnetic field ($\boldsymbol{H}_{\mathrm{stray}}$) it produces, is given by (Brown, 1963):

$$\phi_{\mathrm{stray}} = -\frac{\mu_0 M_{\mathrm{S}}}{2} \boldsymbol{m} \cdot \boldsymbol{H}_{\mathrm{stray}}, \tag{4}$$

where M_{S} is the saturation magnetisation and μ_0 the permeability of free space. Finally, the energy (ϕ_{external}) due to the magnetostatic interaction of

the ferromagnetic body and an external field ($\boldsymbol{H}_{\text{external}}$) is:

$$\phi_{\text{external}} = -\mu_0 M_{\text{S}} \boldsymbol{m} \cdot \boldsymbol{H}_{\text{external}}. \tag{5}$$

Micromagnetic algorithms are used to find the equilibrium magnetisation ($\boldsymbol{m}$) by minimising the Gibbs free-energy (Hubert and Schäfer, 2000). Here, a modified gradient-descent method is used (Ó Conbhuí et al., 2018). The non-local problem of calculating the stray field is handled via a hybrid finite-element/boundary-element formulation (Fredkin and Koehler, 1990). Numerical solutions require a discretisation of the spatial domain into a grid or mesh with a finite number of points on which numerical solutions are calculated. A FEM is used in MERRILL where three-dimensional space is decomposed into tetrahedral pieces called finite elements with the vertices of these elements called the nodes. On each mesh node, a unit vector is initially defined to create an initial guess; the micromagnetic algorithm then attempts to minimise the magnetic Gibbs free-energy by varying the orientation of each vector while ensuring that they remain unitary.

To model greigite at room temperature, we use the same parameters as outlined in Valdez-Grijalva et al. (2018b,a), which are: (1) $M_{\text{S}} = 2.7 \times 10^5$ A/m (Li et al., 2014), (2) $A = 2 \times 10^{-12}$ J/m (Chang et al., 2008), and (3) $K_1 = -1.7 \times 10^4$ J/m^3 (Winklhofer et al., 2014). To model nonuniform structures it is sufficient that the spatial discretisation in the model is always smaller than the exchange length $l_{\text{exch}} = \sqrt{2A/\mu_0 M_{\text{S}}^2}$ (Hubert and Schäfer, 2000), which for greigite is $l_{\text{exch}} \approx 6.6\,\text{nm}$; a maximum element size of 5 nm was chosen here for all meshes.

Truncated-octahedral particles were chosen for the model geometry because authigenic greigite particles typically have such morphology (Snowball,

1997; Roberts et al., 2011), and truncated-octahedral solids can efficiently tessellate 3D space and, thus, produce the close-packed geometries observed in framboidal greigite (Fig. 1). Touching grains are theoretically problematic to model because inter-grain exchange coupling is not well understood. Here, a vanishing exchange coupling is assumed. Framboidal geometries with small gaps (~2 nm) between particles were used, so the only inter-particle interaction is magnetostatic. Particles within a framboid are assigned the same magnetocrystalline anisotropy orientation. In nature, framboids exist where constituent particles are aligned and also randomly aligned (Ohfuji et al., 2006).

In this study we consider the behaviour of individual framboids and ensembles of randomly oriented framboids. In an ensemble of randomly oriented particles/framboids, there are equal probabilities of finding particles with any orientation within an area element of the unit sphere. To simulate a randomly oriented dispersion of identical particles efficiently, it is necessary to model a number of applied field directions (equivalently, particle orientations with respect to the applied field) each of which is representative of a given area on the unit sphere. Given the cubic symmetry of the modelled framboidal cluster geometries (Fig. 1) it is sufficient to simulate the effects of field orientations on the spherical triangle delimited by $(1,0,0)$, $(1/\sqrt{3},1/\sqrt{3},1/\sqrt{3})$, $(0,0,1)$ (Valdez-Grijalva and Muxworthy, 2019; Valdez-Grijalva et al., 2018a). Then, the spherical triangle is subdivided into roughly equal trianglular sub-units to obtain 85 triangular cells; this was found to accurately represent a random distribution over the whole sphere. Each cell represents a field orientation, with the coordinates of the centre of the cell used as the field direction. The

weighted average (cell area)/4π) uses the cell area as the weight for each field direction, and is used to calculate the response for each field orientation as an approximation to the total magnetic response of a framboid ensemble.

2.2. The FORC model

FORCs are a set of partial hysteresis curves obtained from magnetisation states on the upper branch of the hysteresis loop for different field values B_a (Pike et al., 1999; Roberts et al., 2000). For a given B_a and $M(B_a)$, the field $B = B_b$ is increased to positive saturation to trace a magnetisation curve. This procedure is repeated for a number of B_a values to create a magnetisation function with two variables $M = M(B_a, B_b)$ for $B_b \geq B_a$. The FORC distribution ρ is then defined as (Pike et al., 1999; Roberts et al., 2000):

$$\rho = -\frac{\mu_0^2}{2}\frac{\partial^2 M}{\partial B_a \partial B_b}. \tag{6}$$

Contour plots of the FORC distribution are called FORC diagrams and have been used extensively as a proxy for the magnetic domain state and magnetic reversal behaviour of a variety of systems (e.g., Pike et al., 2001; Dumas et al., 2007; Zhao et al., 2017). The standard method to calculate FORC distributions (eqn. 6) is to perform least-squares fitting of a second-degree polynomial surface $M(B_a, B_b) = a_0 + a_1 B_a + a_2 B_b + a_3 B_a B_b + a_4 B_a^2 + a_5 B_b^2 + e$, where e is a collection of error terms, on a sub-grid of the magnetisation function $M(B_a, B_b)$ including $(2 \times \mathrm{SF} + 1)^2$ points in the vicinity of (B_a, B_b) as determined by the smoothing factor SF (Pike et al., 1999); if the magnetisation is approximated in this manner, calculation of eqn. (6) yields $\rho = -\mu_0^2 a_3/2$. Other fitting algorithms have also been developed (e.g., Harrison and Fein-

berg, 2008; Egli, 2013; Egli and Winklhofer, 2014), but here we adopt the original approach of Pike et al. (1999). We use SF = 2 in all figures.

FORC simulations are computationally intensive, so we have developed an approach that reduces the number of calculations required. For each field orientation, the upper hysteresis loop branch is calculated. Most of the curve is traced by the sum of reversible magnetisation motions in each particle in the framboid. Through analysis of > 500 reversible/irreversible processes during hysteresis we developed a set of criteria to identify an irreversible process, which meant that FORCs need only be calculated for B_a field values for which at least one particle undergoes an irreversible rotation (switching) (Valdez-Grijalva et al., 2018a; Valdez-Grijalva and Muxworthy, 2019). These criteria were: a) rotation of the magnetisation by 5° or more from one step to the next, and b) a normalised net magnetisation drop > 0.2 from one step to the next. A field of $B_{\max} = 250\,\mathrm{mT}$ was found to saturate the structure. An external field step of 2 mT was used for all calculations. Thus, for each field orientation we calculate 251 FORCs to obtain the FORC signal of a single cluster orientation. The simulations were performed on the Imperial College Research Computing Service HPC cluster and the Terrawulf III cluster at the Australian National University.

3. Results

3.1. Simulated hysteresis and FORC responses of individual framboids

In our models, individual grains within a framboid all have the same orientation with respect to each other (Fig. 1), i.e., all 30 nm particles have the same orientation. Therefore, the FORC response depends on the field

orientation with respect to the framboid.

We consider first the case where the field is close to the framboid easy axis <111>. During hysteresis the magnetic structure of this framboid is saturated at low fields ~ 50 mT, and all of the 30 nm particles in the framboid remain in a SD state (Fig. 2a). Local interaction fields cause the outer particles in the framboid to rotate coherently to minimise stray fields as the applied field decreases. The remanent state is a double magnetic supervortex with a low remanence ~0.1 M_S that is due to the effective magnetic flux-closure (Harrison et al., 2002) (Fig. 3; see Supplementary Materials for animations of these images). The FORC diagram for this easy axis orientation has a positive peak at $B_c \approx 80$ mT, ~ 5 mT above the $B_u = 0$ axis. A negative response of comparable magnitude is situated below and to the left of the distribution peak. The positive peak response corresponds to the large upward jumps experienced by the reversal curve starting at the switching field $B_a \approx -80$ mT as it approaches positive saturation (Fig. 2a). The negative response is caused by irreversible switching of individual particles in the framboid on FORCs with higher B_a values at $B_b \approx 75$ mT. This combination of negative and positive peaks has been reported previously for vortex systems (Pike and Fernandez, 1999; Carvallo et al., 2003; Valdez-Grijalva et al., 2018a). FORC diagrams for these highly artificial numerical systems have many peaks and troughs compared to measurements on natural samples due to the discrete responses of individual grains to local interaction fields. However, a large positive response close to the $B_c = 0$ axis, i.e., $B_c < 20$ mT, is important because it was found for all field orientations.

When the field is applied along the hard axis <100>, the hysteresis and

FORC responses contrast to that of the easy-axis case (Fig. 2). The hysteresis main branches are more rounded, and switching occurs via reversible rotations, i.e., no discrete jumps during the rotation, with the first irreversible switching occurring at ~150 mT on reducing the field from saturation (Fig. 2c). This gives rise to much smaller jumps than observed for the easy-axis aligned model (Fig. 2a). The main peaks in the FORC diagram (Fig. 2d) are closer to the $B_c = 0$ axis, i.e., $B_c < 20$ mT, than in Fig. 2b.

3.2. Simulated hysteresis and FORC response of framboidal clusters

Averaging the response for all 85 field orientations results in a set of partial hysteresis curves, i.e., the raw FORCs, which are smooth and lack any discrete jumps (Fig. 4a). The saturation remanence (M_{RS}) normalised by M_{S} for the framboid ensemble is $M_{\mathrm{RS}}/M_{\mathrm{S}} \approx 0.1$ and the coercive force is $B_{\mathrm{C}} \approx 5$ mT; this contrasts sharply with the remanence and coercive force of a non-interacting ensemble of isolated SD greigite particles of the same size that have $M_{\mathrm{RS}}/M_{\mathrm{S}} \approx 0.86$ and $B_{\mathrm{C}} \approx 24$ mT (Valdez-Grijalva et al., 2018a). Lower values for framboids are due to magnetostatic interactions among the constituent particles, and formation of super-vortex states (Fig. 3). The minimum field required to saturate the magnetisation, i.e., to make it uniform in a given direction is 150 mT.

The main feature of the simulated FORC diagram for an ensemble of framboidal clusters (Fig. 4b) is a large response centered roughly at $B_c = 10$ mT and $B_u = 0$ mT and two lobes roughly at $B_c = 10$ mT and $B_u = \pm 40$ mT. These features are part of a larger, continuous signal, as highlighted by the box in Fig. 4b. Negative and smaller positive responses lie in a region to the right of this rectangle; however, these features are only ~20% of the

magnitude of the peak response at maximum, and at most are $< 10\%$ of the peak FORC distribution value.

3.3. Hysteresis of larger framboids

An attempt was made to simulate FORC diagrams for framboids consisting of assemblages of greigite particles, which when isolated are in the SV state, i.e., >70 nm. Computational memory and calculation time constraints meant that the FORC response of these framboids with larger particles could not be simulated. Instead, we performed hysteresis simulations of framboids composed of fifteen larger particles ($d = 76\,\mathrm{nm}$) (compared to 65 particles in Section 3.2), which are are in the SV state when isolated (Valdez-Grijalva et al., 2018a,b). We modelled only 40 field orientations. When a saturating field of 250 mT is applied close to the easy axis, the magnetic structure remains nearly uniform until the field is reduced to ~50 mT (Fig. 5; see Supplementary Materials for an animation of these images). As the field is further decreased, outer particles in the framboid nucleate hard-aligned single-vortices (Fig. 5a). The remanent state (Fig. 5b) has a super-vortex structure in which most particles are individually in a two-domain state with clearly defined domain walls (Fig. 5b, green). This state is similar to the easy-aligned SV state exhibited by large >200 nm particles (Valdez-Grijalva et al., 2018b) with six easy aligned domains curling around the vortex core. In this super-vortex structure, outer particles are in a two-domain state and the six easy aligned magnetic domains span multiple particles. Non-interacting 76 nm particles nucleate vortices in the remanence state (Valdez-Grijalva et al., 2018a); however, for this field orientation, the innermost particle in the cluster always remains in a SD state due to internal magnetostatic inter-

actions (Fig. 5b, grey line). This is likely true for larger framboids because relatively more grains will be inside the framboid and the number of grains at the edge of the framboid that experience lower inter-grain magnetostatic interaction fields will be reduced. Grains inside the framboid are more likely to be in a SD state. This suggests that for larger framboids composed of many larger particles, the FORC signal could be similar to that of framboids composed of SD particles (Section 3.2).

4. Discussion

The FORC response of an anisotropic framboidal cluster depends strongly on the orientation of the framboid relative to the applied field. When the field is aligned with an easy axis (<111>) the peak signal lies on the $B_u = 0$ axis at $B_c \approx 80$ mT (Fig. 2b). When the FORC response is averaged over 85 applied field directions, the main feature in the FORC diagrams is a vertical, almost-continuous feature in the box defined by $B_c \approx 0$ to 10 mT and $B_u \approx -60$ mT to 60 mT (Fig. 4b).

Remanence states for all simulated framboid configurations are super-vortex states (Figs. 3 and 5). Super-vortex states form to create flux-closure, akin to closure domains in multidomain systems. These super-vortex states reduce the net magnetisation of each framboid, which means that inter-framboidal interactions are likely weak even when multiple framboids occur relatively close to each other as is often observed in nature (e.g., Roberts, 2015). The saturation-remanence net magnetic moment of the simulated framboid ensemble deviates from the applied field direction by ~12°; this deviation is due to due a combination of inter-grain magnetostatic interaction

fields and magnetocrystalline anisotropy. This observation raises the possibility that framboidal greigite may not carry meaningful palaeomagnetic directions; however, given the low number of particles within framboids (65) and the low number of directions (85) used to determine the net magnetisation direction, further numerical framboidal studies are needed to resolve this issue.

For framboids composed of 30 nm particles, i.e., particles that are in the SD state when isolated, all individual particles in a framboid are SD. The remanence state for framboids consisting of 76 nm particles consists of SD structures for innermost particles, whilst outer particles contribute to what appear to be domain wall-like structures (Fig. 5). Inter-grain and internal magnetostatic interaction fields within the framboid with 76 nm particles appear to give rise to similar net structures to those found for ~200 nm isolated greigite grains, where domain-wall structures begin to initiate (Valdez-Grijalva et al., 2018b).

The FORC response of a simulated clustered greigite ensemble (Fig. 4) contrasts with that of isolated SD and SV grains (Valdez-Grijalva et al., 2018a). Isolated SD greigite particles produce FORC signals with a characteristic boomerang shape, strong $B_u = 0$ contributions and a tilted negative ridge, while SV grains produce a more complex pattern. For isolated SD and SV grains, the FORC response is dominated by irreversible switching, which is evident in raw hysteresis/FORC data. In contrast, for framboidal greigite, the ensemble raw data are smooth (Fig. 4a), i.e., there are no preferred coercivities at which irreversible jumps occur in all or many field directions.

The simulated FORC diagram for framboidal greigite (Fig. 4b) is similar

to that for MD particles (Pike et al., 2001; Muxworthy and Dunlop, 2002). These similarities occur because greigite framboids have especially MD-like behaviour because there are no exchange interactions between individual constituent grains. Exchange interactions tend to hinder MD behavior which is characterized by optimal flux closure.

4.1. Combining the FORC responses of framboids and isolated grains

If we compare the FORC response of framboid clusters made up of 30 nm grains to that of an ensemble of isolated 30 nm grains determined by Valdez-Grijalva et al. (2018a), we find that the peak value of the FORC distribution is substantially smaller: $25.6\times10^{-9}\,\mathrm{m^4A^{-1}kg^{-1}}$ compared to $531.6\times10^{-9}\,\mathrm{m^4A^{-1}kg^{-1}}$, respectively. For an assemblage of 80 nm SV particles the peak value of the FORC distribution is $387.9\times10^{-9}\,\mathrm{m^4A^{-1}kg^{-1}}$ (Valdez-Grijalva et al., 2018a). Therefore, for nearly equal mixtures of framboids and isolated particles, the latter will dominate the FORC response. We demonstrate this dominance in Fig. 6, where we combine FORC model results from Valdez-Grijalva et al. (2018a) for isolated particles with our framboid results. We consider two scenarios: (1) the FORC response of framboids with that of isolated greigite particles in the SD size range 30–48 nm (Fig. 6a), and (2) framboids with isolated particles in the SV grain size range 70–80 nm (Fig. 6b); in both cases the framboidal contribution has been enhanced by adding five times as much by mass compared to the isolated particles. The size distribution of isolated particles is constant. In the first case, isolated particles have SD behaviour, and in the second case only SV behaviour (Valdez-Grijalva et al., 2018a). The mixture of framboidal and isolated SD greigite particles (Fig. 6a) is dominated by the isolated SD signal; however, the framboidal

signal close to the $B_c = 0$ axis is represented clearly in the FORC space, although the less intense framboidal FORC features (Fig. 4b) are hidden by the SD signal. When the signals of isolated SV particles and framboids are combined (Fig. 6b), the FORC response is again dominated by the isolated particles. The framboidal and SV responses mostly overlap and plot within the same area, i.e., close to the B_U axis; however, the framboidal signal is more dominant in the positive B_u region of the diagram.

Based on visual comparisons, simulated FORC responses for mixtures of framboidal and isolated SD grains (Fig. 6a) are similar to those of framboidal-greigite-rich samples from Taiwan obtained by Chou et al. (2012), but are less similar to the FORC response typically identified for greigite (e.g., Rowan and Roberts, 2006; Roberts et al., 2018b). The samples from Chou et al. (2012) might be atypical because they were heated during a fault slip event, whereas most other greigite-rich samples have not been subjected to heat. Therefore, it would appear that the FORC diagrams reported by Rowan and Roberts (2006) and many others represent non-framboidal interacting particle systems; however, electron microscopy observations reveal the presence of framboidal greigite (e.g., Rowan and Roberts, 2006; Roberts et al., 2011). This apparent disconnect between observed and simulated FORC responses might be explained by several mechanisms: (1) alteration of greigite to pyrite on crystal surfaces (and *vice versa*) as observed by Ebert et al. (2018). If crystal surfaces are altered to a non-magnetic phase, e.g., pyrite, this would increase the effective distance between magnetic particles and reduce magnetic interactions to give rise to reduced vertical spreading in FORC diagrams (Muxworthy et al., 2004), but would produce high coerciv-

ities similar to those observed for isolated particles. This means that FORC diagrams could potentially hold information about the degree of pyritisation of a greigite-rich sample. (2) In nature, framboids are rarely as tightly packed as those modelled, i.e., particle sizes and orientations are less uniform which would result in relatively greater particle separation within framboids (Ohfuji and Rickard, 2005; Rickard, 2019). Hüsing et al. (2009) demonstrated that greigite can occur as framboids, non-framboidal masses, and as isolated particles in the same system. Such systems will give rise to higher coercivity FORC diagrams. (3) Many magnetic studies that are combined with electron microscopy might have focused on identifying the presence of framboids, which may not be representative of the bulk magnetic response.

4.2. Framboidal hysteresis behaviour and the "Day" plot

The "Day plot" (Day et al., 1977) is a graph of $M_{\mathrm{RS}}/M_{\mathrm{S}}$ versus $B_{\mathrm{CR}}/B_{\mathrm{C}}$, where B_{CR} is the coercivity of remanence. We determined B_{CR} from the FORC simulations, therefore we estimated it from FORCs that crossed the near the origin, rather than from a series of minor hysteresis loops, which is the standard method of calculating B_{CR}. Despite the many factors that can contribute to ambiguity in interpreting data distributions in the Day diagram (Roberts et al., 2018a), hysteresis parameters are sensitive to domain state variations for particles of a single size, which is one case in which data distributions on the Day plot can be interpreted more clearly (Fig. 7). We also include in Fig. 7 results from Valdez-Grijalva et al. (2018a) for isolated particles, and for the mixtures described in Section 4.1. All calculations are for randomly oriented particle distributions. Data for isolated particles with a defined grain size follow a well-documented trend in the Day plot, as

particles transition from the SD to the SV state (Muxworthy et al., 2003). The framboidal signal and that of mixtures of framboidal and isolated greigite crystals follow a contrasting trend. This is primarily because the framboidal signal contributes to M_S but less significantly to M_{RS}, which gives rise to low M_{RS}/M_S ratios. Increasing contents of isolated SD or SV particles have contrasting effects on the Day plot: increasing the SD content increases the remanence and decreases B_{CR}/B_C, whereas, increasing the SV content has little effect on M_{RS}/M_S while initially decreasing B_{CR}/B_C, before increasing it. The contrasting data positions for the different particle types and mixtures indicate that other processes also contribute to ambiguity in interpreting data distributions in the Day plot as suggested by Roberts et al. (2018a).

5. Conclusions

The FORC response of simulated framboidal greigite ensembles has been calculated with a micromagnetic algorithm. Framboidal greigite clusters that consist of interacting SD particles have similar FORC responses to MD grains. Even though the FORC response has been calculated for framboids that consist of 30 nm SD particles that have stable behaviour when isolated, these observations are likely to hold for framboids composed of larger grains because it is to be expected that such tightly packed particles will produce MD-like FORC signals. Greigite is found to occur commonly with other iron sulphides like pyrite (Rowan and Roberts, 2006; Rowan et al., 2009), and it is uncommon to find large, MD greigite grains. This means that if a sample is known to contain greigite, MD-like FORC signals could be due to framboidal or other forms of strongly interacting greigite.

Acknowledgments

This research was funded by the Instituto Mexicano del Petróleo (M. A. Valdez-Grijalva), National Science Foundation Grant No. EAR1827263 (L. Nagy), NERC grant NE/J020508/1 (A. R. Muxworthy and W. Williams), and Australian Research Council grant DP160100805 (A. P. Roberts and A. R. Muxworthy). The Terrawulf III cluster is supported through the AuScope Australian Geophysical Observing System (AGOS) and the Australian National Collaborative Research Infrastructure Strategy (NCRIS). Model results will be made available on FigShare up on acceptance of this paper.

References

References

Ariztegui, D., Dobson, J., 1996. Magnetic investigations of framboidal greigite formation: a record of anthropogenic environmental changes in eutrophic Lake St. Moritz, Switzerland. Holocene 6, 235–241. URL: https://doi.org/10.1177/095968369600600209, doi:10.1177/095968369600600209.

Brown, W.F., 1963. Micromagnetics. Interscience, New York.

Carvallo, C., Muxworthy, A.R., Dunlop, D.J., Williams, W., 2003. Micromagnetic modeling of first-order reversal curve (FORC) diagrams for single-domain and pseudo-single-domain magnetite. Earth Planet. Sci. Lett. 213, 375–390. URL: https://doi.org/10.1016/S0012-821X(03)00320-0, doi:10.1016/S0012-821X(03)00320-0.

Chang, L., Roberts, A.P., Tang, Y., Rainford, B.D., Muxworthy, A.R., Chen, Q., 2008. Fundamental magnetic parameters from pure synthetic greigite (Fe_3S_4). J. Geophys. Res. 113. URL: https://doi.org/10.1029/2007JB005502, doi:10.1029/2007JB005502.

Chou, Y.M., Song, S.R., Aubourg, C., Song, Y.F., Boullier, A.M., Lee, T.Q., Evans, M., Yeh, E.C., Chen, Y.M., 2012. Pyrite alteration and neoformed magnetic minerals in the fault zone of the Chi-Chi earthquake (M_w7. 6, 1999): evidence for frictional heating and co-seismic fluids. Geochem. Geophys. Geosyst. 13. URL: https://doi.org/10.1029/2012GC004120, doi:10.1029/2012GC004120.

Day, R., Fuller, M., Schmidt, V.A., 1977. Hysteresis properties of titanomagnetites: grain-size and compositional dependence. Phys. Earth Planet. Inter. 13, 260–267. URL: https://doi.org/10.1016/0031-9201(77)90108-X, doi:10.1016/0031-9201(77)90108-X.

Dumas, R.K., Li, C.P., Roshchin, I.V., Schuller, I.K., Liu, K., 2007. Magnetic fingerprints of sub-100 nm Fe dots. Phys. Rev. B 75, 134405. URL: https://doi.org/10.1103/PhysRevB.75.134405, doi:10.1103/PhysRevB.75.134405.

Ebert, Y., Shaar, R., Emmanuel, S., Nowaczyk, N., Stein, M., 2018. Overwriting of sedimentary magnetism by bacterially mediated mineral alteration. Geology 46, 291–294. URL: https://doi.org/10.1130/G39706.1, doi:10.1130/G39706.1.

426 Egli, R., 2013. VARIFORC: An optimized protocol for calculating non-
427 regular first-order reversal curve (FORC) diagrams. Global Planet. Change
428 110, 302–320. doi:10.1016/j.gloplacha.2013.08.003.

429 Egli, R., Winklhofer, M., 2014. Recent developments on processing and
430 interpretation aspects of first-order reversal curves (FORC). Proc. Kazan
431 Univ. Nat. Sci. 156, 14–53.

432 Emmerton, S., Muxworthy, A.R., Sephton, M.A., Aldana, M.,
433 Costanzo-Alvarez, V., Bayona, G., Williams, W., 2013. Cor-
434 relating biodegradation to magnetization in oil bearing sed-
435 imentary rocks. Geochim. Cosmochim. Acta 112, 146–
436 165. URL: https://doi.org/10.1016/j.gca.2013.03.008,
437 doi:10.1016/j.gca.2013.03.008.

438 Fredkin, D.R., Koehler, T.R., 1990. Hybrid method for comput-
439 ing demagnetizing fields. IEEE Trans. Magn. 26, 415–417. URL:
440 https://doi.org/10.1109/20.106342, doi:10.1109/20.106342.

441 Harrison, R.J., Dunin-Borkowski, R.E., Putnis, A., 2002. Direct imaging of
442 nanoscale magnetic interactions in minerals. Proc. Natl. Acad. Sci. USA
443 99, 16556–16561. URL: https://doi.org/10.1073/pnas.262514499,
444 doi:10.1073/pnas.262514499.

445 Harrison, R.J., Feinberg, J.M., 2008. FORCinel: An improved algo-
446 rithm for calculating first-order reversal curve distributions using locally
447 weighted regression smoothing. Geochem. Geophys. Geosys. 9. URL:
448 https://doi.org/10.1029/2008GC001987, doi:10.1029/2008GC001987.

Hubert, A., Schäfer, R., 2000. Magnetic Domains: The Analysis of Magnetic Microstructures. Springer, Berlin.

Hüsing, S.K., Dekkers, M.J., Franke, C., Krijgsman, W., 2009. The Tortonian reference section at Monte dei Corvi (Italy): evidence for early remanence acquisition in greigite-bearing sediments. Geophys. J. Int. 179, 125–143. URL: https://doi.org/10.1111/j.1365-246X.2009.04301.x, doi:10.1111/j.1365-246X.2009.04301.x, arXiv:http://oup.prod.sis.lan/gji/article-pdf/17

Landau, L.D., Lifshitz, E., 1935. On the theory of the dispersion of magnetic permeability in ferromagnetic bodies. Phys. Z. Sowjetunion 8, 101–114.

Li, G., Zhang, B., Yu, F., Novakova, A.A., Krivenkov, M.S., Kiseleva, T.Y., Chang, L., Rao, J., Polyakov, A.O., Blake, G.R., de Groot, R.A., Palstra, T.T.M., 2014. High-purity Fe_3S_4 greigite microcrystals for magnetic and electrochemical performance. Chem. Mater. 26, 5821–5829. URL: https://doi.org/10.1021/cm501493m, doi:10.1021/cm501493m.

Muxworthy, A.R., Dunlop, D.J., 2002. First-order reversal curve (FORC) diagrams for pseudo-single-domain magnetites at high temperature. Earth Planet. Sci. Lett. 203, 369–382. URL: https://doi.org/10.1016/S0012-821X(02)00880-4, doi:10.1016/S0012-821X(02)00880-4.

Muxworthy, A.R., Heslop, D., Williams, W., 2004. Influence of magnetostatic interactions on first-order-reversal-curve (FORC) diagrams: a micromagnetic approach. Geophys. J. Int. 158, 888–

897. URL: https://doi.org/10.1111/j.1365-246X.2004.02358.x, doi:10.1111/j.1365-246X.2004.02358.x.

Muxworthy, A.R., Williams, W., Roberts, A.P., Winklhofer, M., Chang, L., Pósfai, M., 2013. Critical single domain grain sizes in chains of interacting greigite particles: implications for magnetosome crystals. Geochem. Geophys. Geosyst. 14, 5430–5441. URL: https://doi.org/10.1002/2013GC004973, doi:10.1002/2013GC004973.

Muxworthy, A.R., Williams, W., Virdee, D., 2003. Effect of magnetostatic interactions on the hysteresis parameters of single-domain and pseudo-single-domain grains. J. Geophys. Res 108. URL: https://doi.org/10.1029/2003JB002588, doi:10.1029/2003JB002588.

Ó Conbhuí, P., Williams, W., Fabian, K., Ridley, P., Nagy, L., Muxworthy, A.R., 2018. MERRILL: Micromagnetic Earth Related Robust Interpreted Language Laboratory. Geochem. Geophys. Geosyst. 19, 1080–1106. URL: https://doi.org/10.1002/2017GC007279, doi:10.1002/2017GC007279.

Ohfuji, H., Rickard, D., 2005. Experimental syntheses of framboids – a review. Earth-Sci. Rev. 71, 147 – 170. URL: http://www.sciencedirect.com/science/article/pii/S001282520500019X, doi:https://doi.org/10.1016/j.earscirev.2005.02.001.

Ohfuji, H., Rickard, D., Light, M.E., Hursthouse, M.B., 2006. Structure of framboidal pyrite: a single crystal X-ray diffraction study. Eur. J. Min. 18, 93–98. URL: https://doi.org/10.1127/0935-1221/2006/0018-0093, doi:10.1127/0935-1221/2006/0018-0093, arXiv:https://pubs.geoscienceworld.org/eurjmin

Pike, C., Fernandez, A., 1999. An investigation of magnetic reversal in submicron-scale Co dots using first order reversal curve diagrams. J. Appl. Phys. 85, 6668–6676. URL: https://doi.org/10.1063/1.370177, doi:10.1063/1.370177.

Pike, C.R., Roberts, A.P., Dekkers, M.J., Verosub, K.L., 2001. An investigation of multi-domain hysteresis mechanisms using FORC diagrams. Phys. Earth Planet. Inter. 126, 11–25. URL: https://doi.org/10.1016/S0031-9201(01)00241-2, doi:10.1016/S0031-9201(01)00241-2.

Pike, C.R., Roberts, A.P., Verosub, K.L., 1999. Characterizing interactions in fine magnetic particle systems using first order reversal curves. J. Appl. Phys. 85, 6660–6667. URL: https://doi.org/10.1063/1.370176, doi:10.1063/1.370176.

Rickard, D., 2019. Sedimentary pyrite framboid size-frequency distributions: A meta-analysis. Palaeogeogr. Palaeoclimatol. Palaeoecol. 522, 62–75. URL: https://doi.org/10.1016/j.palaeo.2019.03.010, doi:10.1016/j.palaeo.2019.03.010.

Roberts, A.P., 2015. Magnetic mineral diagenesis. Earth-Sci. Rev. 151, 1–47. URL: https://doi.org/10.1016/j.earscirev.2015.09.010, doi:10.1016/j.earscirev.2015.09.010.

Roberts, A.P., Chang, L., Rowan, C.J., Horng, C.S., Florindo, F., 2011. Magnetic properties of sedimentary greigite (Fe_3S_4): an update.

Rev. Geophys. 49. URL: https://doi.org/10.1029/2010RG000336, doi:10.1029/2010RG000336.

Roberts, A.P., Heslop, D., Zhao, X., Pike, C.R., 2014. Understanding fine magnetic particle systems through use of first-order reversal curve diagrams. Rev. Geophys. 52, 557–602. URL: https://doi.org/10.1002/2014RG000462, doi:10.1002/2014RG000462.

Roberts, A.P., Pike, C.R., Verosub, K.L., 2000. First-order reversal curve diagrams: a new tool for characterizing the magnetic properties of natural samples. J. Geophys. Res. 105, 28461–28475. URL: https://doi.org/10.1029/2000JB900326, doi:10.1029/2000JB900326.

Roberts, A.P., Tauxe, L., Heslop, D., Zhao, X., Jiang, Z., 2018a. A critical appraisal of the Day diagram. J. Geophys. Res.: Solid Earth 123, 2618–2644. URL: https://doi.org/10.1002/2017JB015247, doi:10.1002/2017JB015247, arXiv:https://agupubs.onlinelibrary.wiley.com/doi/pdf/10.1002/2017JB015247.

Roberts, A.P., Zhao, X., Harrison, R.J., Heslop, D., Muxworthy, A.R., Rowan, C.J., Larrasoaña, J.C., Florindo, F., 2018b. Signatures of reductive magnetic mineral diagenesis from unmixing of first-order reversal curves. J. Geophys. Res.: Solid Earth 123, 4500–4522. URL: https://doi.org/10.1029/2018JB015706, doi:10.1029/2018JB015706, arXiv:https://agupubs.onlinelibrary.wiley.com/doi/pdf/10.1029/2018JB015706.

Rowan, C.J., Roberts, A.P., 2006. Magnetite dissolution, diachronous greigite formation, and secondary magnetizations from

pyrite oxidation: unravelling complex magnetizations in Neogene marine sediments from New Zealand. Earth Planet. Sci. Lett. 241, 119–137. URL: https://doi.org/10.1016/j.epsl.2005.10.017, doi:10.1016/j.epsl.2005.10.017.

Rowan, C.J., Roberts, A.P., Broadbent, T., 2009. Reductive diagenesis, magnetite dissolution, greigite growth and paleomagnetic smoothing in marine sediments: a new view. Earth Planet. Sci. Lett. 277, 223–235. URL: https://doi.org/10.1016/j.epsl.2008.10.016, doi:10.1016/j.epsl.2008.10.016.

Snowball, I.F., 1997. Gyroremanent magnetization and the magnetic properties of greigite-bearing clays in southern Sweden. Geophys. J. Int. 129, 624–636. URL: https://doi.org/10.1111/j.1365-246X.1997.tb04498.x, doi:10.1111/j.1365-246X.1997.tb04498.x.

Valdez-Grijalva, M.A., Muxworthy, A.R., 2019. First-order reversal curve (FORC) diagrams of nanomagnets with cubic magnetocrystalline anisotropy. J. Magn. Magn. Mater. 471, 359–364. URL: https://doi.org/10.1016/j.jmmm.2018.09.086, doi:10.1016/j.jmmm.2018.09.086.

Valdez-Grijalva, M.A., Muxworthy, A.R., Williams, W., Ó Conbhuí, P., Nagy, L., Roberts, A.P., Heslop, D., 2018a. Magnetic vortex effects on first-order reversal curve (FORC) diagrams for greigite dispersions. Earth Planet. Sci. Lett. 501, 103–111. URL: https://doi.org/10.1016/j.epsl.2018.08.027, doi:10.1016/j.epsl.2018.08.027.

563 Valdez-Grijalva, M.A., Nagy, L., Muxworthy, A.R., Williams, W., Fabian,
564 K., 2018b. The magnetic structure and palaeomagnetic recording
565 fidelity of sub-micron greigite (Fe_3S_4). Earth Planet. Sci. Lett.
566 483, 76–89. URL: https://doi.org/10.1016/j.epsl.2017.12.015,
567 doi:10.1016/j.epsl.2017.12.015.

568 Winklhofer, M., Chang, L., Eder, S.H.K., 2014. On the magnetocrys-
569 talline anisotropy of greigite (Fe_3S_4). Geochem. Geophys. Geosyst.
570 15, 1558–1579. URL: https://doi.org/10.1002/2013GC005121,
571 doi:10.1002/2013GC005121.

572 Zhao, X., Roberts, A.P., Heslop, D., Paterson, G.A., Li, Y., Li,
573 J., 2017. Magnetic domain state diagnosis using hysteresis rever-
574 sal curves. J. Geophys. Res.: Solid Earth 122, 4767–4789. URL:
575 https://doi.org/10.1002/2016JB013683, doi:10.1002/2016JB013683.

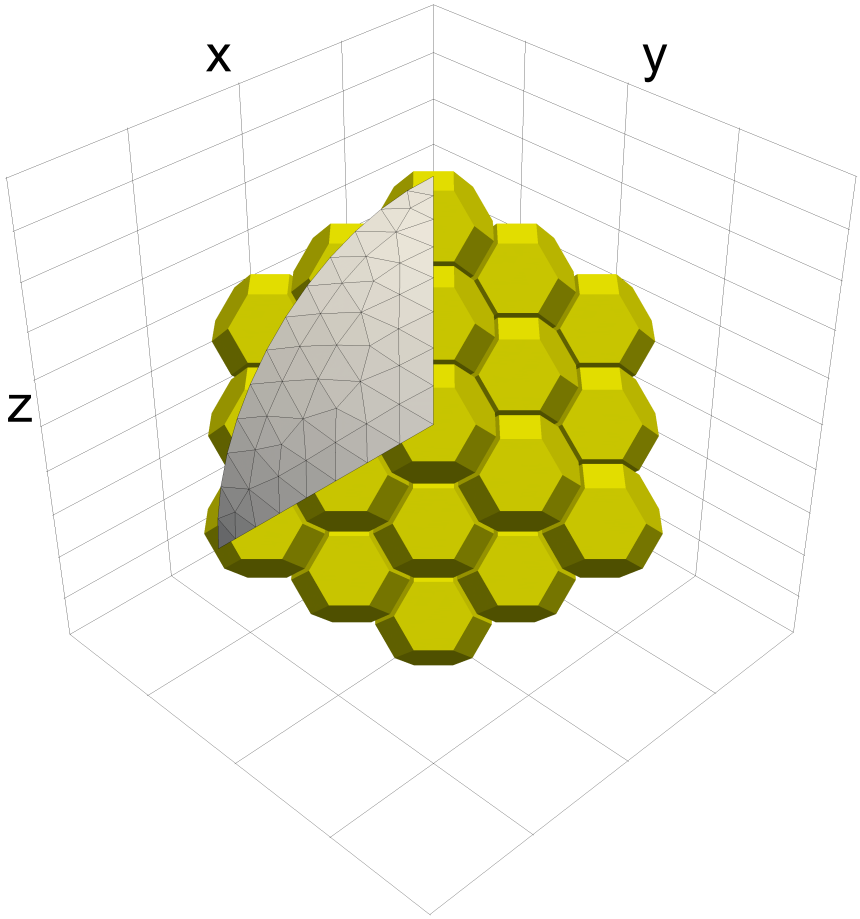

Figure 1: Framboidal mesh and field orientations. Field orientations are obtained from a triangular mesh over the spherical triangle delimited by $(1, 0, 0)$, $(1/\sqrt{3}, 1/\sqrt{3}, 1/\sqrt{3})$, $(0, 0, 1)$. Given the cluster symmetry, this region contains all field orientations of interest. The framboid contains 65 truncated octahedral particles each with size $d = 30$ nm. The small gap between particles is $\sim$2 nm. The grey mesh contains an illustration of the angles over which the 85 directions were calculated.

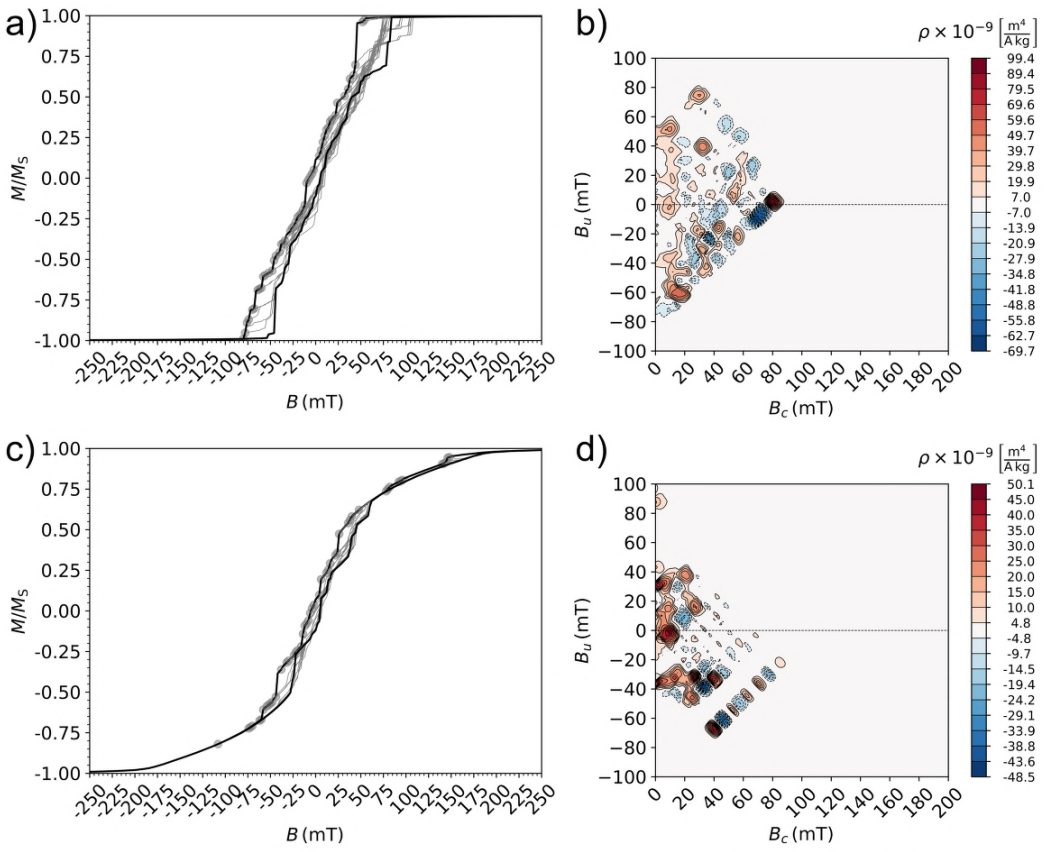

Figure 2: FORCs and FORC diagrams for framboidal greigite clusters with 30 nm crystallites for fields along an (a, b) easy and a (c, d) hard axis. When the field is aligned close to an easy axis, there is a peak FORC response on the $B_u = 0$ axis at $B_c \approx 80$ mT (b). For fields close to the hard axis, the FORC response has a peak at $B_c \approx 10$ mT (d). SF = 2 for both FORC diagrams.

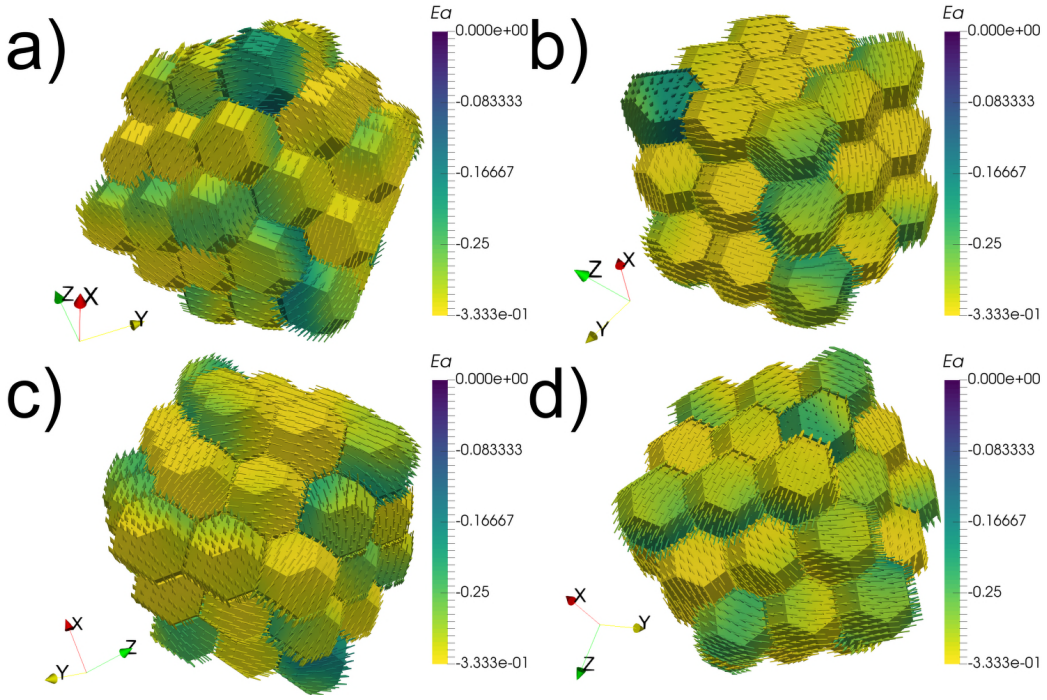

Figure 3: Various framboid saturation-remanence magnetic states (super-vortex states). For fields (a) close to an easy axis, (b) close to a hard axis, (c) close to a saddle point, and (d) close to an intermediate direction between the easy, hard, and saddle point directions. There are 85 applied field orientations in total. The net magnetic moment of the total ensemble is ~12° from the applied field. See supplementary material for short animations of these images.

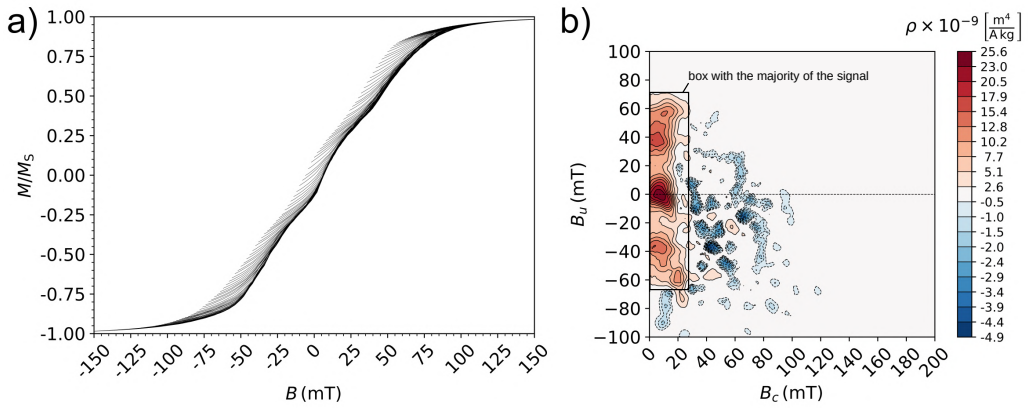

Figure 4: Simulated FORCs for the greigite framboid dispersion. The framboids consist of 65 particles aligned identically and with equal size $d = 30$ nm. (a) When averaged over the 85 field directions, the raw hysteresis/FORCs are smooth, and (b) the FORC response is MD-like (SF = 2). The box discussed in the text is highlighted in b.

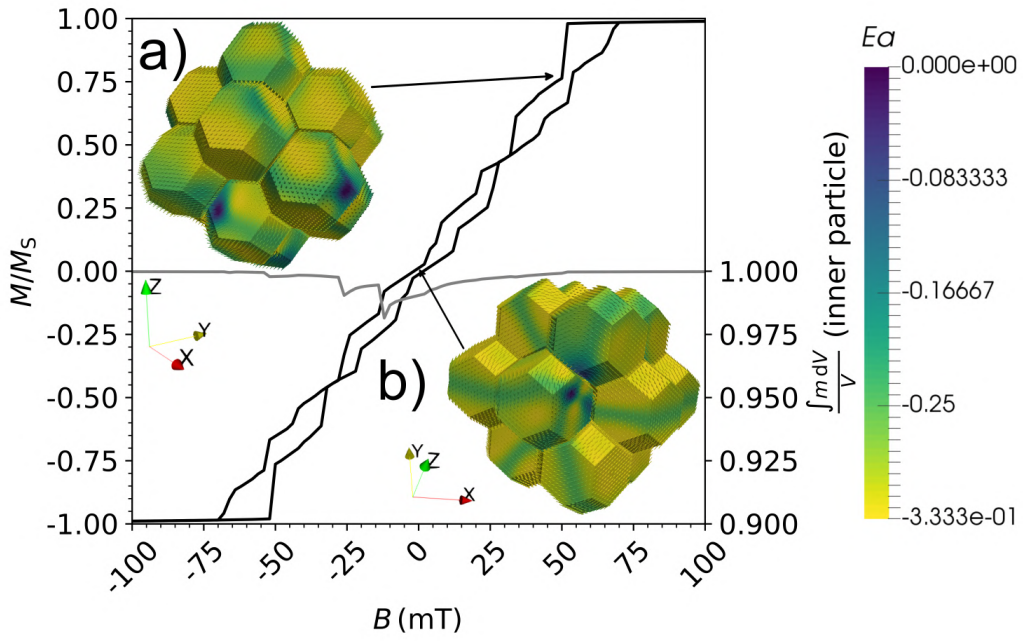

Figure 5: Hysteresis loop for a framboid with 76 nm particles for a field aligned close to the easy-anisotropy axis. Due to numerical limitations, the framboid consists of only 15 crystallites. On reducing the field from saturation, (a) the magnetisation remains saturated to ~50 mT when a few particles nucleate vortices. (b) The remanent state is a super-vortex structure with most particles in a two-domain-like state. Domain walls are visible as thin, green regions. The grey line is the reduced magnetisation of the middle particle within the framboid during reduction of the external field. The right-hand vertical axis is the reduced magnetisation; the closer the magnetisation is to one, the greater SD the magnetic structure during hysteresis. Values below ~0.8 (on the right-hand axis) start to display non-SD-like structures. The middle particle switches direction between ~-15 and -25 mT.

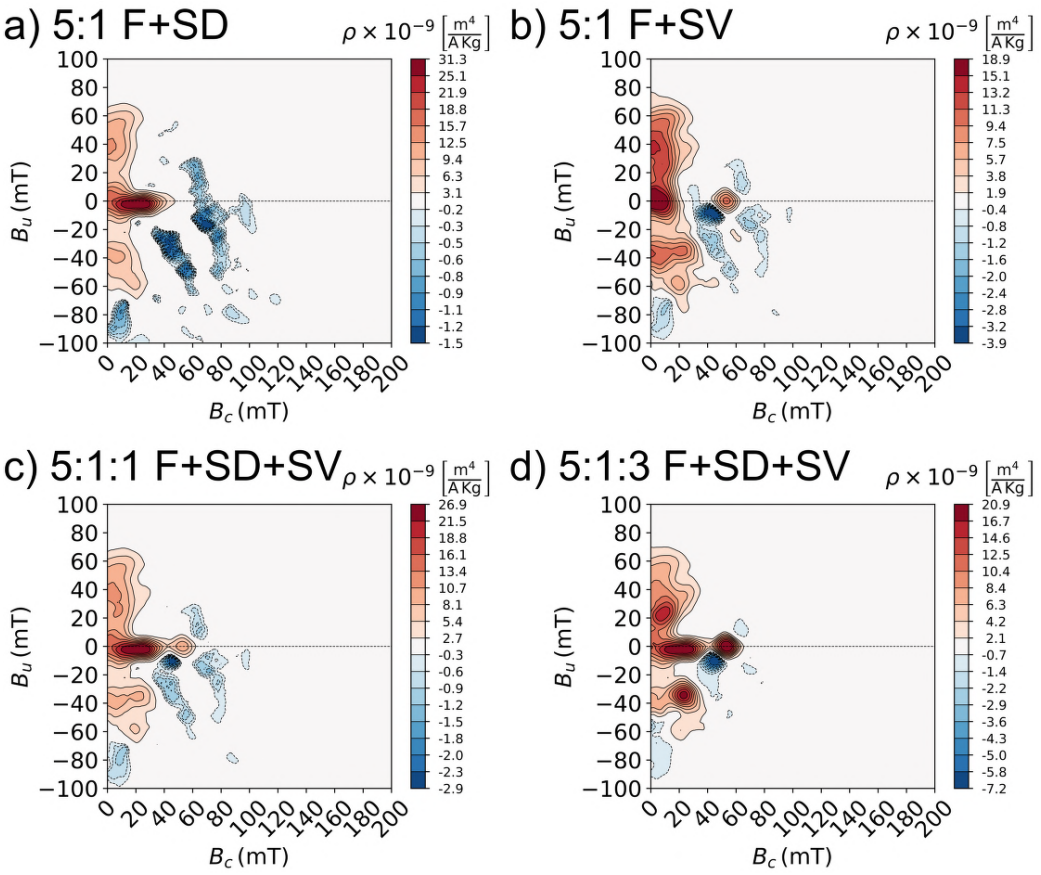

Figure 6: Simulated FORC diagrams for dispersions of framboids mixed with isolated particles. In (a) isolated particles are all in the SD size range (30–48 nm), and in (b) SV particles are modelled in the size range 70–80 nm. The framboidal (F), SD and SV simulations are mixed in varying proportions: (a) 5:1 F:SD, (b) 5:1 F:SV, (c) 5:1:1 F:SD:SV and (d) 5:1:3 F:SD:SV. SF = 2 in all FORC diagrams. The signal is dominated by the non-interacting particles because the framboidal signal is weaker per unit mass. The framboidal signal is still visible because it occupies regions that the isolated particles do not. Solutions for isolated particles are taken from Valdez-Grijalva et al. (2018a).

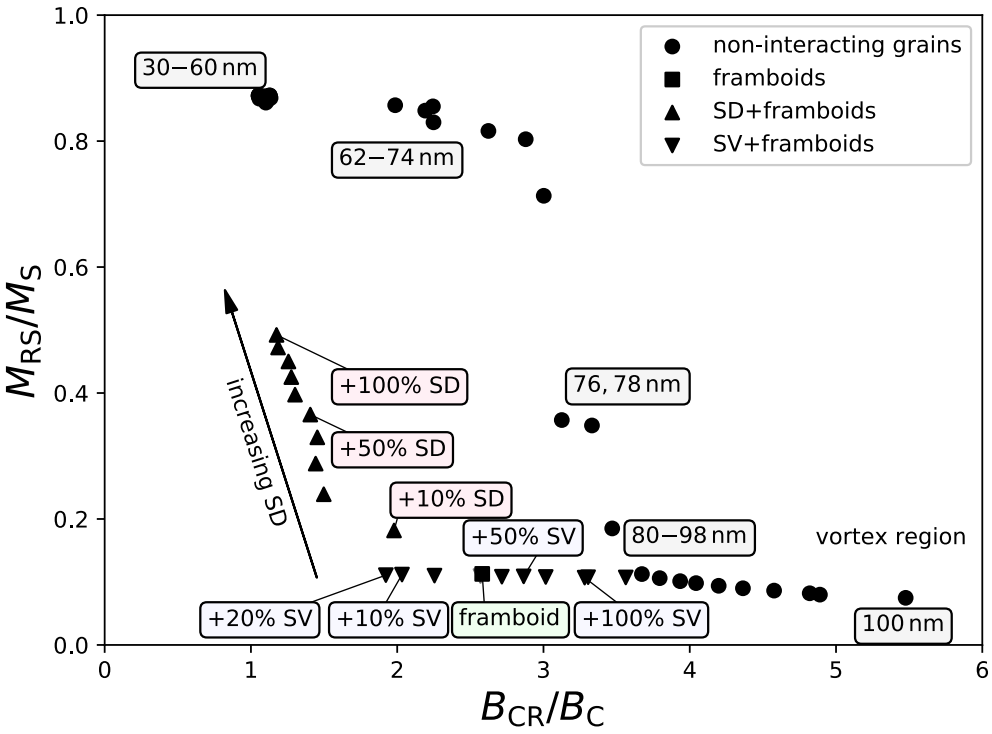

Figure 7: Day plot with simulation results for individual grains of different sizes, the framboid with 30 nm particles, mixtures of framboids with isolated SD grains (upward-pointing triangles), and isolated SV grains (downward-pointing triangles). The mixtures contain increasing proportions of SD and SV material, ranging from 10% to 100% by mass of the framboid contribution. SD contributions consist of grains in the 30-48 nm size range, and SV grains in the 70-80 nm range. Solutions for isolated particles are from Valdez-Grijalva et al. (2018a). All simulations are for distributions of randomly oriented particles.